Article

Thermoelectric Grain Boundary in Monolayer MoS$_2$

Ayu Irie, Anikeya Aditya, Ken-ichi Nomura, Shogo Fukushima, Shinnosuke Hattori, Rajiv K. Kalia, Aiichiro Nakano, Vadim Rodin, Fuyuki Shimojo, Shigetaka Tomiya, and Priya Vashishta*

Cite This: https://doi.org/10.1021/acs.jpcc.4c04339

Read Online

ACCESS | 📊 Metrics & More | 📑 Article Recommendations | 🆂ℹ Supporting Information

ABSTRACT: Defects such as grain boundaries (GBs) fundamentally control thermal and electrical transport in two-dimensional (2D) transition metal dichalcogenide (TMDC) materials, but the mechanism remains elusive. We have studied thermal and electrical transport across and along the GB within a monolayer of a prototypical TMDC, MoS$_2$, using molecular dynamics simulation and first-principles quantum-mechanical calculation. We found the existence of an interfacial phase (or "interphase") within a few nanometers from the GB, which has anisotropic transport properties that are distinct from those of a perfect crystal. Namely, the GB interphase has reduced thermal conductivity across the GB. In stark contrast, the electrical conductivity of electron-doped MoS$_2$ is enhanced in both directions, with higher conductivity across the GB. These results are understood in terms of the alignment of energy levels and spatial distribution of electronic wave functions around the GB. Such contrasting thermal and electrical transport properties of the GB interphase suggest a promising application of GB superlattices to thermoelectric power regeneration for sustainable future 2D electronics.
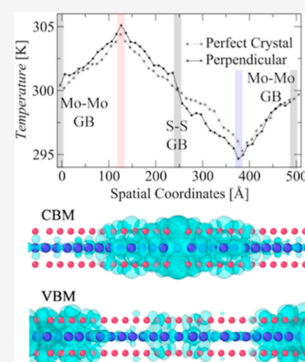
INTRODUCTION

Atomically thin van der Waals materials[1] have emerged as a breakthrough platform to potentially extend Moore's law of electronics, where transition metal dichalcogenide (TMDC) materials act as key semiconductors.[2,3] In the coming age of two-dimensional (2D) electronics, the electrical conductivity of a doped TMDC plays an essential role for future semiconductor devices,[4] while their thermal conductivity is critical for energy harvesting devices based on the thermo-electric effect.[5]

Among TMDCs, monolayer MoS$_2$ has garnered significant attention due to its remarkable optoelectronic[6−10] and thermal[11] properties. Its 2D structure gives rise to distinct physical properties compared with its bulk form. Monolayer MoS$_2$ has a direct band gap of 1.8 eV, making it suitable for optoelectronic applications such as photodetectors and light-emitting diodes.[6] Its high carrier mobility also allows for swift electron movement, making it advantageous for high-speed electronic devices. These exceptional characteristics have propelled extensive research on monolayer MoS$_2$, holding promise for potential electronics and energy conversion applications.

Defects such as grain boundaries (GBs) greatly influence the structural, mechanical, thermal, electronic,[12] and magnetic[13] properties of monolayer MoS$_2$, notably thermoelectric performance.[4,5] Studies have demonstrated that doping MoS$_2$ GBs with transition metals can lower their formation energies, resulting in induced magnetism and enhanced electron mobilities.[14] Furthermore, research has revealed that the size of MoS$_2$ grains influences the performance of MoS$_2$ transistors, with devices featuring larger grains in the channel region

exhibiting improved on/off current ratios due to reduced carrier scattering from GBs.[15] These findings suggest that the meticulous engineering of GBs in monolayer MoS$_2$ holds the potential for enhancing its thermoelectric performance.

Here, we study the effects of low-energy GBs composed of 5- and 7-membered rings on thermal and electrical transport in monolayer MoS$_2$. We first perform nonequilibrium molecular dynamics (NEMD) simulations[11] to calculate thermal conductivity based on Fourier's law. We then calculate the electrical conductivity of electron-doped MoS$_2$ using the Kubo−Greenwood formula[16] in the framework of density functional theory (DFT).[17]

METHODS

Thermal Conductivity. We use NEMD simulations[11] based on reactive force field (ReaxFF)[18] to compute the thermal conductivity. Simulations are performed on a square monolayer MoS$_2$ crystal with a side $L = 500$ Å with periodic boundary conditions (PBCs) along the lateral (x and y) directions, while a large vacuum is inserted in the vertical (z) direction to avoid spurious interaction between periodic images. We define heat source and sink regions each of 1 nm width at $x = L/4$ and $3L/4$, respectively (Figure S1 in the

Supporting Information). To establish steady heat flux density J_Q, a fixed energy flux $\dot{Q}$ is added to (or subtracted from) the kinetic energy of atoms in the source (or sink) region. After the initial transient, this establishes a temperature gradient ∇T between the two regions. Thermal conductivity κ is then computed from the Fourier law, $J_Q = -\kappa \nabla T$.

Electrical Conductivity. We compute electrical conductivity across and along the GB using the Kubo−Greenwood formula[16] in the framework of DFT.[17] Electron doping is achieved by adding electrons corresponding to a specified doping level while adding uniform background charge to maintain charge neutrality. Our QXMD code[19] computes optical conductivity tensor elements

$$\sigma_{\alpha\alpha}(\omega) = \frac{2\pi e^2 \hbar^2}{m^2 \omega V} \sum_{\mathbf{k}} W_{\mathbf{k}} \sum_{m,n} (f_{m,\mathbf{k}} - f_{n,\mathbf{k}}) |\langle \psi_{n,\mathbf{k}} | \nabla_\alpha | \psi_{m,\mathbf{k}} \rangle|^2 \delta$$

$$(\varepsilon_{n,\mathbf{k}} - \varepsilon_{m,\mathbf{k}} - \hbar\omega) \tag{1}$$

and DC conductivity is obtained by its zero-frequency limit, $\omega \rightarrow 0$. In eq 1, $\alpha \in \{x,y\}$; e and m are the charge and mass of an electron, respectively; $\hbar$ is the Planck constant; V is the volume of the system; $|\psi_{n,\mathbf{k}}\rangle$, $\varepsilon_{n,\mathbf{k}}$, and $f_{n,\mathbf{k}}$ are the wave function, energy, and occupation number of the Kohn−Sham eigenstate of the n-th band with wave vector $\mathbf{k}$; and $W_{\mathbf{k}}$ is the k-point weighting factor. For numerical computation, Fermi distribution with a temperature 9300 K is used for $f_{n,\mathbf{k}}$ while Gaussian broadening of 0.8 eV is applied to the delta function $(\varepsilon_{n,\mathbf{k}} - \varepsilon_{m,\mathbf{k}} - \hbar\omega)$. The electronic states are calculated using the projector augmented wave method.[20,21] Projector functions are generated for the 4d and 5s states of Mo and the 3s and 3p states of S, respectively. The generalized gradient approximation is used for the exchange−correlation energy.[22] The van der Waals interaction between atoms is described in the DFT-D approach.[23] The momentum−space formalism is utilized, where the plane-wave cutoff energies are 40 and 200 Ry for the electronic pseudowave functions and pseudocharge density, respectively. The GB system contains 78 Mo and 156 S atoms, while the perfect crystal consists of 60 Mo and 120 S (Figure S2). We used the Γ point for both systems without and with GB.

■ RESULTS AND DISCUSSION

Thermal Conductivity. We first perform NEMD simulations to calculate the thermal conductivity of the MoS$_2$ monolayer with and without the GB at a temperature of 300 K. For the GB system, we insert symmetric 5−7 GBs consisting of 5- and 7-membered rings, which have low energies and are expected to be prominent in MoS$_2$ crystals.[24] Due to PBCs, this creates two types of GBs—Mo−Mo and S−S GBs—which are characterized, respectively, by the presence of S−S and Mo−Mo homobonds at the center and end of the simulation cell (Figures 1 and S3 in the Supporting Information).

We use NEMD simulations[11] based on reactive force field (ReaxFF)[24] to compute thermal conductivity. ReaxFF was adopted because of its ability to describe Mo−Mo and S−S bonds in GBs, which cannot be described by the previously used Stillinger−Weber force field.[11,25] To establish steady heat flux density J_Q, a fixed energy flux $\dot{Q}$ is added to (or subtracted from) the heat source (or sink) region (Figures 1 and S1 in the Supporting Information). After initial transient, this establishes a temperature gradient ∇T between the two regions. Thermal conductivity κ is then computed from the Fourier law, $J_Q =$
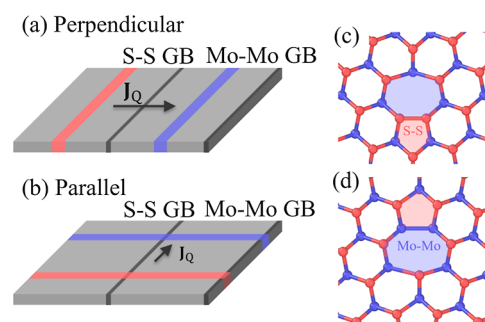

Figure 1. Thermal conductivity calculation with GBs in monolayer MoS$_2$. Computation of (a) perpendicular ($\kappa_\perp$) and (b) parallel ($\kappa_\parallel$) thermal conductivities, including the S−S GB (c) and Mo−Mo GB (d). In (a, b), GBs at the center and end of the simulation cell are colored dark gray, whereas heat source and sink are colored red and blue, respectively.

$-\kappa \nabla T$. To compute perpendicular ($\kappa_\perp$) and parallel ($\kappa_\parallel$) thermal conductivities, heat sources and sinks are placed in such a way that the heat flux is across and along the GBs, respectively (Figure 1).

We first perform NEQMD simulations for perfect MoS$_2$ crystal with a square-shaped simulation cell with side $L = 50$ nm, containing 28,574 Mo and 57,148 S atoms. Figure S4a in the Supporting Information shows the temperature profile averaged over 1.75 ns after 0.3 ns of thermalization. Due to PBCs, there are two physically equivalent sides between the heat source and sink that have respective temperature gradients (labeled sides 1 and 2 in Figure S4a). Average over the linear fits of both sides (Figure S4b, c, respectively) give 6.3 ± 0.2 W/(m·K) for a perfect crystal. This value is close to that obtained using a different force field in ref 11, thus validating the current study. While the absolute value of thermal conductivity calculated using MD simulations is sensitive to the choice of force fields and often deviates from experimentally observed values,[26] effects of structural defects such as isotopes and voids are systematic within the same force field and physically explainable.[11,25] As such, we expect that the observed trends in our results are robust.

We next studied thermal transport across GBs to compute the perpendicular thermal conductivity $\kappa_\perp$ as in Figure 1a. In this case, there are two distinct sides, one containing the S−S GB and the other containing the Mo−Mo GB (Figure 2a). We see rapid temperature drops around the two GBs (marked by gray stripes in Figure 2a), which indicates the existence of GB interfacial phases (or interphases).[27−30] The best fits for interphase thermal conductivity and width yield are as follows: $\kappa_\perp^{S-S} = 1.4$ W/(m·K) and $\kappa_\perp^{Mo-Mo} = 1.6$ W/(m·K) for perpendicular GB-interphase thermal conductivity; see Figures S5 and S6 in the Supporting Information for details and further discussion on sample size dependence of thermal conductivity. This magnitude relationship is consistent with findings from prior research.[12] Additionally, the GB interphase width values are $L_{S-S} = 3.8$ and $L_{Mo-Mo} = 4.3$ nm. Namely, the perpendicular thermal conductivity across the GB is much lower than the perfect crystal value (6.3 ± 0.2 W/(m·K)) in both GB interphases, where the S−S GB has a slightly lower thermal conductivity. The reduced thermal conductivity is likely due to enhanced phonon scattering across the GB. While a few nanometer-thick equilibrium interphases with distinct thermodynamic properties from those of the bulk have been well established,[27−30] we are not aware of nonequilibrium
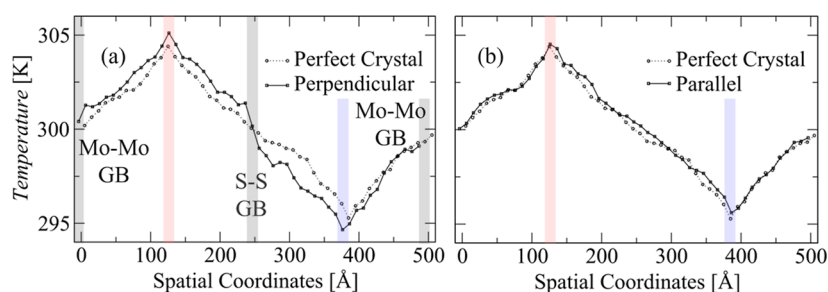
Figure 2. Temperature profile (a) perpendicular and (b) parallel to GBs. Black and gray symbols show results with and without GBs, respectively. Gray stripes represent GB interphases, while red and blue stripes signify the heat source and sink, respectively.

interphases with distinct transport properties in the literature. GB contribution to thermal conductivity is commonly interpreted as thermal boundary conductance assuming zero interphase width and step function temperature drop.[5,31] For the GBs in the current study, in contrast, the sharp but finite slope within a few nanometers (which is an order of magnitude larger than atomic bond lengths) from the GB in Figure 2a is better understood by the nonequilibrium GB interphase concept.

The situation is in marked contrast for thermal conductivity $\kappa_\parallel$ that is calculated for thermal flux along the GB as in Figure 1b. Figure S7a in the Supporting Information shows the calculated temperature profile. Due to PBCs, there are again two physically equivalent sides between the heat source and sink that develop a temperature gradient (sides 1 and 2 in Figure S7a). Average over the linear fits of both sides (Figure S7b, c) gives an effective parallel thermal conductivity of $\kappa_\parallel^{\text{effective}} = 6.3 \pm 0.2$ W/(m·K), which is a weighted sum of the perfect crystal value κ and the parallel thermal conductivity $\kappa_\parallel$ of the interphases

$$\kappa_\parallel^{\text{effective}} = \frac{L_{\text{S−S}} + L_{\text{Mo−Mo}}}{L}\kappa_\parallel + \frac{L - (L_{\text{S−S}} + L_{\text{Mo−Mo}})}{L}\kappa \tag{2}$$

By solving eq 2 for $\kappa_\parallel$ gives $\kappa_\parallel = 6.3$ W/(m K), a value close to the perfect crystal value (6.3 ± 0.2 W/(m·K)). This is consistent with the nearly identical temperature profiles with and without GBs in Figure 2b. The nearly identical $\kappa_\parallel$ value to the bulk thermal conductivity is also consistent with the calculated temperature distribution in Figure S8 and in the Supporting Information. Namely, temperature distribution near GBs does not show clear difference from that in the rest of the system.

Table I summarizes the anisotropic thermal conductivities across and along GBs. Thermal conductivities across the GB

Table I. Thermal Conductivity of Monolayer MoS$_2$ for Perfect Crystal and Those of the GB Interphase across and along the GB

κ [W/(m·K)]	$\kappa_\perp$ [W/(m·K)]	$\kappa_\parallel$ [W/(m·K)]
6.3 ± 0.2	1.4 ($\kappa_\perp^{\text{S−S}}$)	6.3
	1.6 ($\kappa_\perp^{\text{Mo−Mo}}$)	

are notably lower than the crystalline value, indicating that the GB serves as an additional scattering center for heat flux in that direction. Conversely, thermal transport along the GB remains unaffected and maintains an identical value to the crystal.

Electrical Conductivity. We next compute the electrical conductivity of doped MoS$_2$ across and along the GB using the Kubo−Greenwood formula[16] in the framework of DFT.[17] Systems with and without the GB are shown in Figure S2 and in the Supporting Information. Since MoS$_2$ is a native n-type semiconductor, we consider electron doping in the range of 0− 2% of the number of valence electrons. After relaxing atomic positions to the minimum energy configuration, a single-point self-consistent field calculation is performed to calculate electrical conductivity.

Figure 3 compares the calculated electrical conductivity as a function of the electron doping concentration for both
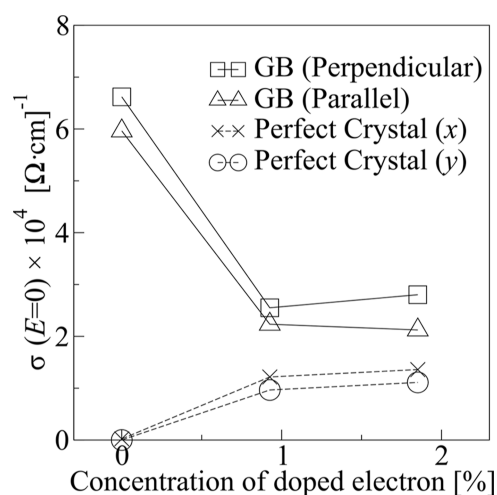

Figure 3. Electrical conductivity as a function of electron doping level. DC conductivity $\sigma_{\alpha\alpha}(0)(\alpha\in\{x,y\})$ is plotted for perfect crystalline (circles and crosses), perpendicular to GB (squares), and parallel to GB (triangles). To mitigate the arbitrary impact of Gaussian broadening in the Kubo−Greenwood formula during practical calculations of the delta function, all data were normalized by subtracting the value of the undoped perfect crystal.

perpendicular and parallel to the GB as well as that for a perfect crystal. Generally, the systems with GBs exhibit higher electrical conductivity than those with a perfect crystal. Even without electron doping, the system with a GB displays a nonzero electrical conductivity of $6.3 \times 10^4/\Omega\cdot$cm. Moreover, the electrical conductivity in the system with a GB is found to be anisotropic, with the conductivity perpendicular to the GB, $\sigma_\perp$, being higher compared to that parallel to GB, $\sigma_\parallel$. Specifically, $\sigma_\perp$ is approximately $0.6 \times 10^4/\Omega\cdot$cm higher than $\sigma_\parallel$. It should be noted that the simulated doping level is higher than typical experimental values due to the small system size; see Figure S9 in the Supporting Information for further discussion on sample size dependence of the electrical conductivity. For example, 1% doping corresponds to a carrier

concentration of 1.8×10^{14} cm^{-2}, whereas the experimental carrier concentration of monolayer MoS$_2$ typically falls within the range of 1.2 to 2.3×10^{12} cm^{-2}.[32] Electrical conductivity enhancement due to the GB at experimental doping levels is expected to be between those at 0% and 1% doping, as shown in Figure 3.

To understand the electronic mechanism underlying the enhanced electrical conductivity at GBs, Figure 4 compares the
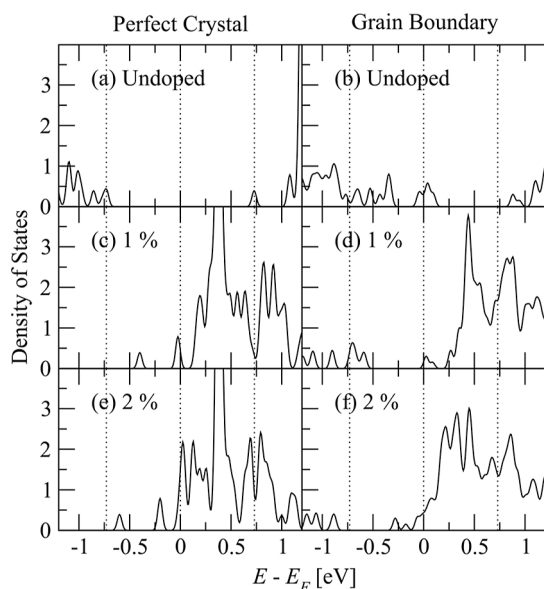
Figure 4. Electronic DoS of (a, c, and e) perfect crystal and (b, d, and f) GB systems. (a, b) are undoped, (c, d) are 1% electron-doped, and (e, f) are 2% electron-doped. The dotted lines represent the valence band maximum (VBM) and the conduction band minimum (CBM) of the perfect crystal and the Fermi level, respectively.

electronic density of states (DoSs) for undoped and doped systems with and without GBs. In contrast to perfect crystals, which exhibits a band gap near the Fermi energy without doping (thus zero electrical conductivity), systems with GBs reveal defect-induced midgap levels and more continuous distribution of states. The continuous DoS is likely the origin of the higher electrical conductivity observed in the GB systems. To better understand the character of electronic states, Figure S10 in the Supporting Information shows partial DoS. The DoS predominantly arises from the 4d orbital of Mo and the 3p orbital of S. Notably, the 5s orbital of Mo has much denser population within the conduction band in the GB system compared to the perfect crystal.

To investigate the nature of electronic wave functions near the Fermi level, Figure 5 shows the isosurfaces of wave functions just below and above the Fermi level of 1% electron-doped systems. Wave functions are localized around GBs in both the VBM and CBM. Specifically, the VBM wave function predominantly localizes around Mo−Mo GBs, with reduced presence around the S−S GB and the pristine area. In contrast, the VBM wave functions strongly localize around the S−S GB, with reduced presence around the Mo−Mo GB and the pristine area. As a result, the wave functions of occupied and unoccupied states are distributed nonuniformly and alternately perpendicular to the GB, while they are uniformly distributed parallel to the GB. This nonuniform distribution of wave functions of occupied and unoccupied states is the origin of
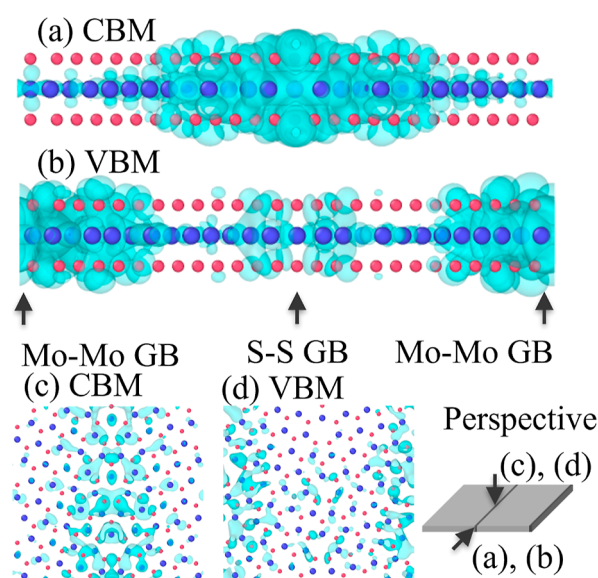
Figure 5. Electronic wave function. Isosurfaces of Kohn−Sham wave functions at the valence band minimum (b, d) and conduction band minimum (a, c) for the GB system. (a, b) are front view, whereas (c, d) are top view.

large matrix elements $|\langle \Psi_{\text{occupied},\mathbf{k}} | \nabla_\alpha | \Psi_{\text{unoccupied},\mathbf{k}} \rangle|^2$ in the Kubo−Greenwood formula, leading to the observed anisotropy in electrical conductivity. This suggests enhanced electrical conductivity, especially across the GB, when GBs are aligned with an interval of a few nanometers. Figure S11 in the Supporting Information shows electronic orbital contributions to the KS bands. We observe the dominance of Mo 4d and S 3p orbitals across most bands in both GB and perfect crystal systems. What is notable is a higher degree of hybridization between these two orbitals within the midgap states of the GB system compared to the perfect crystal. This observation aligns with the isosurface representations of the Kohn−Sham wave functions in Figure 5. Such hybridization indicates distribution of orbitals among both Mo and S within the midgap states, thereby promoting electrical conduction. Also notable is the higher contribution of Mo 5s orbitals within the conduction in the GB system compared to the perfect crystal. Since the Mo 5s orbital has a larger spatial extent compared to the Mo 4d orbital, it has a larger matrix element and hence contributes more to electrical conductivity. Figure S12 in the Supporting Information shows that the radial pseudoatomic wave function of the Mo 5s orbital indeed has a larger magnitude at the nearest-neighbor S atom position compared to the Mo 4d orbital.

Thermopower is known to be temperature-dependent. Thermal conductivity exhibits well-known temperature dependence,[11] which however is insensitive to structural defects.[25] To examine the temperature dependence of electrical conductivity, we have performed new calculations, where the electronic temperature in the Fermi distribution within the Kubo−Greenwood formula varied in the range between 0.1 and 500 K (see Figure S13 in the Supporting Information). We found that electrical conductivity exhibits much weaker temperature dependence than thermal conductivity, where electrical conductivity slightly decreases with increasing temperature. While these should result in temperature-dependent thermopower, effects of structural defects like

GBs discussed in this paper are temperature independent and are expected not to change the temperature dependence of thermopower.

CONCLUSIONS

Calculated thermoelectric conductivities with GBs composed of 5- and 7-membered rings have provided valuable insights. Most importantly, an interphase of approximately 4 nm was found to form GB, which exhibits distinct thermoelectric properties compared from bulk. Thermal conductivity was calculated using NEMD with a reactive force field, revealing a remarkable reduction of approximately 80% across GB compared to perfect crystal. On the contrary, GB does not affect thermal conductivity along GB. Electrical conductivity was calculated using DFT and the Kubo−Greenwood equation. GB enhances electrical conductivity even without doping due to the midgap levels. Specifically, electrical conductivity is larger by 6.6×10^4 and $6.0 \times 10^4/\Omega\cdot$cm, respectively, across and along GB, compared to perfect crystal. This anisotropic electrical conduction in electrical conductivity has been attributed to the alignment of energy levels and the spatial distribution of wave functions around GBs. These findings suggest exciting prospects for applying GBs in thermoelectric applications. Meticulous control of temperature gradient and voltage across GBs makes it possible to concurrently achieve low thermal and high electrical conductivity compared to a perfect crystal. This will, in turn, enable potential utilization of GBs in thermoelectric devices, holding promise for advancing energy conversion technologies. Future research can focus on optimizing and fine-tuning the properties of GBs to maximize their thermoelectric performance and explore their practical applications in various fields. In particular, our results suggest that a superlattice of GBs exhibits excellent thermoelectric properties, which makes it an excellent candidate for power regeneration from wasted heat in microprocessors toward sustainable future electronics (Figure S14 in the Supporting Information).[33] Scalable manufacturing of such superlattices may be facilitated by surface-induced defect self-duplication[34] and stress-induced self-assembly.[35]

ASSOCIATED CONTENT

Ⓢ Supporting Information

The Supporting Information is available free of charge at https://pubs.acs.org/doi/10.1021/acs.jpcc.4c04339.

> Schematic of NEMD simulation, system used for electrical conductivity calculation, GB system construction, temperature profile in pristine MoS_2, temperature profile across GBs, temperature profile across GBs with 1000×500 Å system, temperature profile along GBs, temperature distribution when the heat flux is parallel to GBs, number of k-point samples dependence on electrical conductivity as a proxy for the size effect, electronic partial density of states, electronic orbital contributions to the Kohn−Sham bands, radial pseudoatomic wave functions of Mo and S atoms, temperature dependence on electrical conductivity in the GB system with 1% doping, GB superlattice for thermoelectric power regeneration, and XYZ configuration files (10.5281/zenodo.13345394) (PDF)

AUTHOR INFORMATION

Corresponding Author

Priya Vashishta − *Collaboratory for Advanced Computing and Simulation, Department of Chemical Engineering and Materials Science, Department of Computer Science, and Department of Physics & Astronomy, University of Southern California, Los Angeles, California 90089-0242, United States;* ⓘ orcid.org/0000-0003-4683-429X; Phone: (310) 849-4282; Email: priyav@usc.edu

Authors

Ayu Irie − *Collaboratory for Advanced Computing and Simulation, Department of Chemical Engineering and Materials Science, Department of Computer Science, and Department of Physics & Astronomy, University of Southern California, Los Angeles, California 90089-0242, United States; Department of Physics, Kumamoto University, Kumamoto 860-8555, Japan*

Anikeya Aditya − *Collaboratory for Advanced Computing and Simulation, Department of Chemical Engineering and Materials Science, Department of Computer Science, and Department of Physics & Astronomy, University of Southern California, Los Angeles, California 90089-0242, United States;* ⓘ orcid.org/0000-0001-9533-7666

Ken-ichi Nomura − *Collaboratory for Advanced Computing and Simulation, Department of Chemical Engineering and Materials Science, Department of Computer Science, and Department of Physics & Astronomy, University of Southern California, Los Angeles, California 90089-0242, United States;* ⓘ orcid.org/0000-0002-1743-1419

Shogo Fukushima − *Institute for Materials Research, Tohoku University, Sendai 980-8577, Japan*

Shinnosuke Hattori − *Sony Semiconductor Solutions Corporation, Atsugi, Kanagawa 243-0014, Japan;* ⓘ orcid.org/0000-0003-0786-1308

Rajiv K. Kalia − *Collaboratory for Advanced Computing and Simulation, Department of Chemical Engineering and Materials Science, Department of Computer Science, and Department of Physics & Astronomy, University of Southern California, Los Angeles, California 90089-0242, United States*

Aiichiro Nakano − *Collaboratory for Advanced Computing and Simulation, Department of Chemical Engineering and Materials Science, Department of Computer Science, and Department of Physics & Astronomy, University of Southern California, Los Angeles, California 90089-0242, United States;* ⓘ orcid.org/0000-0003-3228-3896

Vadim Rodin − *Sony Europe B.V., Sony Semiconductor Solutions Europe, Stuttgart Laboratory 2, Stuttgart D-70327, Germany*

Fuyuki Shimojo − *Department of Physics, Kumamoto University, Kumamoto 860-8555, Japan;* ⓘ orcid.org/0000-0002-4025-0069

Shigetaka Tomiya − *Sony Semiconductor Solutions Corporation, Atsugi, Kanagawa 243-0014, Japan; Nara Institute of Science and Technology, Nara 8916-5, Japan*

Complete contact information is available at:
https://pubs.acs.org/10.1021/acs.jpcc.4c04339

Author Contributions

AI performed simulations. AA and KN helped simulation setup and analysis. SF and FS provided simulation techniques. RKK, AN, and PV designed the research. SH, VR, and ST provided

device and application aspects of research. All authors discussed and prepared the manuscript.

Notes

The authors declare no competing financial interest.

■ ACKNOWLEDGMENTS

■ REFERENCES

(1) Geim, A. K.; Grigorieva, I. V. Van der Waals heterostructures. *Nature* **2013**, *499* (7459), 419−425.

(2) Li, M.-Y.; Su, S.-K. H.-S.; Wong, H.-S. P.; Li, L.-J. How 2D semiconductors could extend Moore's law. *Nature* **2019**, *567*, 169−170.

(3) Poddar, P. K.; Zhong, Y.; Mannix, A. J.; Mujid, F.; Yu, J.; Liang, C.; Kang, J.-H.; Lee, M.; Xie, S.; Park, J. Resist-Free Lithography for Monolayer Transition Metal Dichalcogenides. *Nano Lett.* **2022**, *22* (2), 726−732.

(4) Zou, X.; Liu, Y. Z.; Yakobson, B. I. Predicting dislocations and grain boundaries in two-dimensional metal-disulfides from the first principles. *Nano Lett.* **2013**, *13* (1), 253−258.

(5) Lin, C.; Chen, X.; Zou, X. Phonon-grain-boundary-interaction-mediated thermal transport in two-dimensional polycrystallineMoS2. *ACS Appl. Mater. Interface* **2019**, *11* (28), 25547−25555.

(6) Splendiani, A.; Sun, L.; Zhang, Y.; Li, T.; Kim, J.; Chim, C.-Y.; Galli, G.; Wang, F. Emerging photoluminescence in monolayer MoS2. *Nano Lett.* **2010**, *10* (4), 1271−1275.

(7) Lee, Y.; Hu, Y.; Lang, X.; Kim, D.; Li, K.; Ping, Y.; Fu, K.-M. C.; Cho, K. Spin-defect qubits in two-dimensional transition metal dichalcogenides operating at telecom wavelengths. *Nat. Commun.* **2022**, *13* (1), 7501.

(8) Yang, J. A.; Bennett, R. K. A.; Hoang, L.; Zhang, Z.; Thompson, K. J.; Michail, A.; Parthenios, J.; Papagelis, K.; Mannix, A. J.; Pop, E. Biaxial Tensile Strain Enhances Electron Mobility of Monolayer Transition Metal Dichalcogenides. **2023**, arXiv:2309.10939. arXiv [cond-mat.mes-hall].

(9) Raja, A.; Montoya−Castillo, A.; Zultak, J.; Zhang, X.-X.; Ye, Z.; Roquelet, C.; Chenet, D. A.; van der Zande, A. M.; Huang, P.; Jockusch, S.; et al. Energy Transfer from Quantum Dots to Graphene and MoS2: The Role of Absorption and Screening in Two-Dimensional Materials. *Nano Lett.* **2016**, *16* (4), 2328−2333.

(10) Yu, L.; Lee, Y.-H.; Ling, X.; Santos, E. J. G.; Shin, Y. C.; Lin, Y.; Dubey, M.; Kaxiras, E.; Kong, J.; Wang, H.; et al. Graphene/MoS2 Hybrid Technology for Large-Scale Two-Dimensional Electronics. *Nano Lett.* **2014**, *14* (6), 3055−3063.

(11) Krishnamoorthy, A.; Rajak, P.; Norouzzadeh, P.; Singh, D. J.; Kalia, R. K.; Nakano, A.; Vashishta, P. Thermal conductivity of MoS2 monolayers from molecular dynamics simulations. *AIP Adv.* **2019**, *9* (3), 035042.

(12) Bernholc, J.; Nardelli, M. B.; Fattebert, J. L.; Orlikowski, D.; Roland, C.; Rosef, F.; Zhao, Q. Atomic Transformations and Quantum Transport in Carbon Nanotubes. *MRS Online Proc. Libr.* **1999**, *593* (1), 547−557.

(13) Huang, X.; Makmal, A.; Chelikowsky, J. R.; Kronik, L. Size-Dependent Spintronic Properties of Dilute Magnetic Semiconductor Nanocrystals. *Phys. Rev. Lett.* **2005**, *94* (23), 236801.

(14) Qiu, X.; Wang, Y.; Jiang, Y. Dopants and grain boundary effects in monolayer MoS2: a first-principles study. *Phys. Chem. Chem. Phys.* **2021**, *23* (20), 11937−11943.

(15) Lin, C.-P.; Lyu, L.-S.; Lin, C.-T.; Liu, P.-S.; Chang, W.-H.; Li, L.-J.; Hou, T.-H. Grain size effect of monolayer MoS2 transistors characterized by second harmonic generation mapping. In *2015 IEEE22nd International Symposium on the Physical and Failure Analysis of Integrated Circuits*; IEEE, 2015, pp 476−479..

(16) Zhang, Y.; Wang, C.; Zheng, F.; Zhang, P. Quantum molecular dynamics simulations of thermophysical properties of fluid ethane. *Phys. Rev. E* **2012**, *86* (6), 061111.

(17) Hohenberg, P.; Kohn, W. Inhomogeneous electron gas. *Phys. Rev.* **1964**, *136* (3B), B864−B871.

(18) van Duin, A. C. T.; Dasgupta, S.; Lorant, F.; Goddard, W. A. ReaxFF: A Reactive Force Field for Hydrocarbons. *J. Phys. Chem. A* **2001**, *105* (41), 9396−9409.

(19) Shimojo, F.; Fukushima, S.; Kumazoe, H.; Misawa, M.; Ohmura, S.; Rajak, P.; Shimamura, K.; Bassman Oftelie, L.; Tiwari, S. C.; Kalia, R. K.; et al. QXMD: an open-source program for nonadiabatic quantum molecular dynamics. *SoftwareX* **2019**, *10*, 100307.

(20) Blochl, P. E. Projector augmented-wave method. *Phys. Rev. B* **1994**, *50* (24), 17953−17979.

(21) Kresse, G.; Furthmuller, J. Efficient iterative schemes for ab initio total-energy calculations using a plane-wave basis set. *Phys. Rev. B* **1996**, *54* (16), 11169−11186.

(22) Perdew, J. P.; Burke, K.; Ernzerhof, M. Generalized gradient approximation made simple. *Phys. Rev. Lett.* **1996**, *77* (18), 3865−3868.

(23) Grimme, S. Semiempirical GGA-type density functional constructed with a long-range dispersion correction. *J. Comput. Chem.* **2006**, *27* (15), 1787−1799.

(24) Mortazavi, B.; Quey, R.; Ostadhossein, A.; Villani, A.; Moulin, N.; van Duin, A. C. T.; Rabczuk, T. Strong thermal transport along polycrystalline transition metal dichalcogenides revealed by multiscale modeling for MoS2. *Appl. Mater. Today* **2017**, *7*, 67−76.

(25) Baradwaj, N.; Aditya, A.; Mishra, A.; Burns, K.; Lang, E.; Hachtel, J. A.; Hattar, K.; Aitkaliyeva, A.; Nakano, A.; Vashishta, P.; et al. Probing phonon focusing, thermomechanical behavior, and moiré patterns in van der Waals architectures using surface acoustic waves. *npj Comput. Mater.* **2024**, *10* (1), 137.

(26) Kim, S. E.; Mujid, F.; Rai, A.; Eriksson, F.; Suh, J.; Poddar, P.; Ray, A.; Park, C.; Fransson, E.; Zhong, Y.; et al. Extremely anisotropic van der Waals thermal conductors. *Nature* **2021**, *597* (7878), 660−665.

(27) Dillon, S. J.; Tang, M.; Carter, W. C.; Harmer, M. P. Complexion: a new concept for kinetic engineering in materials science. *Acta Mater.* **2007**, *55* (18), 6208−6218.

(28) Baram, M.; Chatain, D.; Kaplan, W. D. Nanometer-thick equilibrium films: the interface between thermodynamics and atomistics. *Science* **2011**, *332* (6026), 206−209.

(29) Szlufarska, I.; Nakano, A.; Vashishta, P. A crossover in the mechanical response of nanocrystalline ceramics. *Science* **2005**, *309* (5736), 911−914.

(30) Shimamura, K.; Shimojo, F.; Kalia, R. K.; Nakano, A.; Vashishta, P. Bonding and structure of ceramic-ceramic interfaces. *Phys. Rev. Lett.* **2013**, *111* (6), 066103.

(31) Sood, A.; Cheaito, R.; Bai, T.; Kwon, H.; Wang, Y. n.; Li, C.; Yates, L.; Bougher, T.; Graham, S.; Asheghi, M.; et al. Direct visualization of thermal conductivity suppression due to enhanced phonon scattering near individual grain boundaries. *Nano Lett.* **2018**, *18* (6), 3466−3472.

(32) Dagan, R.; Vaknin, Y.; Henning, A.; Shang, J. Y.; Lauhon, L. J.; Rosenwaks, Y. Two-dimensional charge carrier distribution in MoS2 monolayer and multilayers. *Appl. Phys. Lett.* **2019**, *114* (10), 101602.

(33) Beretta, D.; Neophytou, N.; Hodges, J. M.; Kanatzidis, M. G.; Narducci, D.; Martin- Gonzalez, M.; Beekman, M.; Balke, B.; Cerretti, G.; Tremel, W.; et al. Thermoelectrics: From history, a window to the future. *Mater. Sci. Eng., R* **2019**, *138*, 100501.

(34) Yuan, Z.; Nakano, A. Self-replicating twins in nanowires. *Nano Lett.* **2013**, *13* (10), 4925−4930.

(35) Aditya, A.; Mishra, A.; Baradwaj, N.; Nomura, K.; Nakano, A.; Vashishta, P.; Kalia, R. K. Wrinkles, ridges, miura-ori, and moire patterns in MoSe2 using neural networks. *J. Phys. Chem. Lett.* **2023**, *14* (7), 1732−1739.